Resistive pulse sensing of magnetic beads and supraparticle structures using tunable pores

Geoff R. Willmott,[1,2,a)] Mark Platt,[3] and Gil U. Lee[3]
[1]*Industrial Research Limited, 69 Gracefield Rd, P.O. Box 31-310, Lower Hutt 5040, New Zealand*
[2]*The MacDiarmid Institute for Advanced Materials and Nanotechnology, Victoria University of Wellington, P.O. Box 600, Wellington 6140, New Zealand*
[3]*School of Chemistry and Chemical Biology, University College Dublin, Belfield, Dublin 4, Ireland*

(Received 28 October 2011; accepted 9 December 2011; published online 12 January 2012)

Tunable pores (TPs) have been used for resistive pulse sensing of 1 μm superparamagnetic beads, both dispersed and within a magnetic field. Upon application of this field, magnetic supraparticle structures (SPSs) were observed. Onset of aggregation was most effectively indicated by an increase in the mean event magnitude, with data collected using an automated thresholding method. Simulations enabled discrimination between resistive pulses caused by dimers and individual particles. Distinct but time-correlated peaks were often observed, suggesting that SPSs became separated in pressure-driven flow focused at the pore constriction. The distinct properties of magnetophoretic and pressure-driven transport mechanisms can explain variations in the event rate when particles move through an asymmetric pore in either direction, with or without a magnetic field applied. Use of TPs for resistive pulse sensing holds potential for efficient, versatile analysis and measurement of nano- and microparticles, while magnetic beads and particle aggregation play important roles in many prospective biosensing applications. © *2012 American Institute of Physics*. [doi:10.1063/1.3673596]

I. INTRODUCTION

When a particle passes through a thin channel filled and surrounded by aqueous electrolyte, there is a transient change in the channel's ionic resistance, known as a "resistive pulse." Resistive pulse sensing, which enables high-throughput analysis of individual micro- and nanoparticles, was developed by Coulter[1] and applied to cell counters. In the 1970s, deBlois and co-workers used resistive pulse sensing to investigate organisms on scales of hundreds of nanometers.[2,3] The recent flourishing of nano- and biotechnologies has sparked renewed interest in dispersed micro- and nanoparticles. In parallel, resistive pulse sensing has been revived, particularly for studies of DNA (Refs. 4–15) following the first report of single-molecule DNA sensing using biological nanopores in 1996.[4]

Consequently, resistive pulse research has diversified over three orders of length scale magnitude, from single molecules to cells.[16] Within this range, many particle types present opportunities for improved characterization or quality control—drug delivery capsules, viruses, functionalized particles for diagnostic assays, blood platelets, emulsions, and magnetic beads are a few important examples. The sophistication of resistive pulse sensing has also increased, making use of channels made from carbon nanotubes,[17,18] glass,[19–23] silicon,[5,8,15,24] polymers,[25–28] and elastomers.[29–38] Resistive pulses can now be used for study and measurement of particle size,[2,3,17,18,20,21,34] concentration,[33] and charge.[17,38] There is clear potential to extend applications towards sensing of complicated dynamic interactions[24] and specific particle shapes.

[a)]Author to whom correspondence should be addressed. Electronic mail: g.willmott@irl.cri.nz. Tel: (64) (0)4 931 3220. Fax: (64) (0)4 931 3754.

In this paper, we report the use of tunable pores (TPs) for resistive pulse sensing of superparamagnetic beads (SPMs). TPs are fabricated by puncturing a thin elastomeric membrane.[29,30] This membrane can be reversibly actuated on macroscopic scales in order to stretch and relax the micro- to nanoscale conical pore geometry.[31] The ionic current passing through a TP can vary by at least an order of magnitude when the pore is stretched.[32] Therefore, any individual pore specimen has considerable versatility relating to the size of particles it can analyze. TPs can be manufactured to target any particular particle type(s) of the order of tens of nanometers or larger, and sensing of individual DNA plasmids has been reported.[29] In addition to particle size,[34] concentration,[33] and charge,[38] TPs have been used to study multimodal particle size distributions,[30,36] surface-modified particles,[36,37] and the effects of solution pH on particle transport.[33] Recently, a semi-analytic approach was developed to simulate resistive pulses in TPs, and this was used to investigate pulse asymmetry.[35] Pore blockages caused by impurities, aggregation, polydispersity, or surface adhesion are an impediment in most resistive pulse experiments. TPs enable removal of blockages by stretching the membrane to allow an oversize particle to pass through the pore or by forced removal when an overpressure is applied on either side of the membrane. In the case of terminal blockages, replacement pores from the same fabrication batch have similar physical characteristics.[31]

SPMs are finding many applications on sub-cellular length scales, especially in biomedical,[39] microfluidic, and microTAS technologies.[40] They are of particular benefit in assay development and biological handling applications, providing an efficient and cost-effective way to separate and pre-concentrate analytes from solutions.[41–44] Their versatility has been demonstrated by use in conjunction with techniques such as the polymerase chain reaction,[45] mass spectroscopy,[46] and high-throughput linear magnetophoresis (LM) assays.[41,47–50] Precise application of magnetic fields has enabled device-based quadrupole sorting,[51–54] active bead transport for biosensing,[55] and dynamic manipulation of magnetic supraparticle structures (SPSs).[56] For applications in which target analytes contain multiple binding sites or epitopes, it is possible for the target to bind to multiple beads simultaneously, leading to aggregation.[41,57–59] Multiple-particle binding has been used in LM, allowing detection of the dengue virus at 10 plaque forming units ml^{-1}.[41] Alternative methods monitor aggregation using chain length,[60] turbidity,[57] or changes in magnetic properties when particles are in close proximity to each other.[58]

The fundamental reason for the high utility of SPMs is that the physics of bead manipulation is independent of usual microfluidic and biological processes.[40] In resistive pulse sensing, physical mechanisms for driving particles through the constriction can be summarized by Nernst-Planck theory, which gives the particle flux through a pore,

$$\mathbf{J} = -D\nabla C + \frac{\epsilon\zeta C}{\eta}\mathbf{E} + C\mathbf{v_c} + \mathbf{J_m}. \quad (1)$$

Here D is the diffusion coefficient, C is the particle concentration, $\mathbf{E}$ is the electric field, and ϵ and η are the solution permittivity and viscosity. Electrophoretic transport follows Smoluchowski's approximation with particle zeta potential ζ, while $\mathbf{v_c}$ and $\mathbf{J_m}$ are the convective flow velocity and the magnetophoretic flux, respectively. From left to right, the terms refer to diffusive, electrophoretic and convective fluxes, with the latter incorporating pressure-driven and electroosmotic flows. The final term, magnetophoresis, is relevant for the case of magnetic beads in an applied magnetic field.

Magnetophoresis has two specific points of difference in comparison with the other transport mechanisms. Firstly, SPMs gain an induced dipole in a magnetic field, generating interparticle forces which cause spontaneous clustering into magnetic SPSs.[40] In resistive pulse experiments using non-magnetic particles, long-range interparticle forces are not significant, so the particles typically remain dispersed. In this case, the duration of a resistive pulse (Δt, roughly equivalent to the time spent by the particle within the pore constriction) is much less than the average time between resistive pulse "events" (T). Secondly, convective and electrophoretic transport are focused at the pore constriction, where flow and electric fields are greatest. In contrast, the

magnetic field is not strongly concentrated in the pore, because the relative permeabilities of non-magnetic materials such as the membrane and the electrolyte are equal to 1, to within 1%.

We study resistive pulse sensing of 1 μm SPMs in the presence of a simple bar magnet. We are not aware of previous publications detailing resistive pulse sensing of magnetic beads in a magnetic field, although magnetoresistive detection of individual beads has been reported.[61] We show how it is possible to control resistive pulse behavior by applying and switching magnetic fields. We study SPSs, recognizing that resistive pulse sensing has high potential for detailed, real-time analysis of particle aggregation. This requires discrimination between clusters of unknown size, shape, and orientation when the time between events may be comparable to the duration of an event ($\Delta t \approx T$). Aggregation is an important issue for diagnostic assays, nanotoxicology[62,63] and the stability of colloidal or emulsified dispersions. Resistive pulse experiments have been used to study aggregation of $\sim$10 μm polystyrene beads,[64] crystals during growth,[65] and amyloids.[66] Here, we take further steps towards cluster analysis in resistive pulse sensing, utilizing the distinct transport properties of magnetic beads.

II. APPARATUS AND EXPERIMENTS

The *qNano* apparatus (Fig. 1(a)) and a tunable pore specimen were supplied by Izon Science (Christchurch, New Zealand). The pore is located within a thin ($\sim$200 μm) membrane at the center of a specimen made from thermoplastic polyurethane (Elastollan 1160D, BASF, Fig. 1(b)). The septum is stretched and relaxed using pegs placed in holes at the ends of four legs of the membrane. Separation between pegs on opposite legs was varied between 45 and 49 mm but is the same across both pairs of legs, so that the strain applied to the septum is predominantly radial.[31] Aqueous electrolyte is contained within upper and lower fluid cells which surround the membrane, and Ag/AgCl electrodes are embedded in each half of the cell.

Commercial polymer-coated magnetic beads (Dynabeads® MyOne, Invitrogen 650-11) of monodisperse diameter 1 μm were suspended in 0.1 M KCl solution at pH 6.1 and concentration 4×10^8 ml^{-1}. The beads have negative electrophoretic mobility due to their carboxyl active chemical functionality of 0.6 mmol g^{-1} of beads (3.6×10^8 groups per bead). Between experiments, the solution containing the beads was ultrasonicated. The fluid cell and membrane were cleaned using deionized water and dried using Kimwipes and in a stream of nitrogen. Solution containing beads was added to the lower fluid cell, and 50 μl of the same solution without beads was added to the upper cell. The TP was oriented so that the lower cell was adjacent to the smaller pore entrance (Fig. 1(c)).

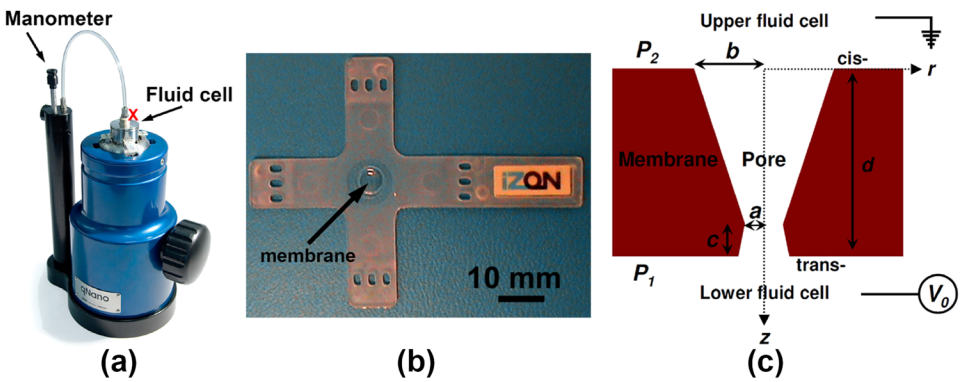

FIG. 1. The setup for tunable pore experiments. (a) The *qNano* apparatus with the specimen, fluid cell, and manometer unit in place. To apply a magnetic field, a small bar magnet was placed on top of the fluid cell, adjacent to the manometer attachment (at the red "x"). (b) The elastomeric specimen, which enables actuation of a pore within the thin central membrane. A schematic cross-section of a pore is shown in (c). A constriction of radius a is located a distance c from the lower membrane surface, and the opening at the upper surface has radius b. The membrane thickness is d, the transmembrane potential is V_0, the downwards pressure head is $P_2 - P_1$, and the r and z co-ordinates of a cylindrical polar co-ordinate system are indicated.

The gravitational pressure in the top half of the cell is approximately 50 Pa,[38] so transport of particles upwards through the pore in zero magnetic field was driven by overpressure applied to the lower fluid cell using a manometer ($P_1 > P_2$, Fig. 1). Although negative potential difference was applied to the lower electrode, pressure-driven flow dominated electrokinetic transport. In our experiments, the minimum ratio of pressure-driven to electrokinetic particle flux can be estimated from Eq. (1) (see Ref. 33) by considering a constriction of the same size as the smaller pore radius ($\sim$2.5 μm) with 20 Pa pressure and $V_0 = -0.1$ V applied, and using a high estimate of $\zeta = -50$ mV on a particle or pore surface. In this extreme case, the flux ratio is greater than 4, and a more typical value (300 Pa pressure applied) is in excess of 50. To induce magnetic transport and chain formation, a permanent magnet was placed on top of the upper fluid cell, approximately 15 mm from the pore. The applied potential was – 0.1 V in all experiments, and ionic current was sampled at 50 kHz and recorded by the *qNano's* instrument control software (v2.1).

A. Columnar magnetic superparamagnetic structures

Columnar magnetic SPSs formed over $\sim$15 s in conditions similar to those used in resistive pulse experiments (Fig. 2). It is known that columnar (or chain-like) SPSs form when beads are placed in a uniform magnetic field,[40] and the response time to magnetic field changes is also consistent with previous work.[61] When the magnetic field was removed, the beads redispersed in the solution. It has been suggested that clusters of $\sim$1 μm beads can remain intact following removal of a field, because the remnant (hysteretic) magnetic bead moment can dominate the thermal energy.[40] Such a calculation does not account for surface chemistries which are designed to maintain stable dispersions. Clusters are also known to break up when they are exposed to shear flows[56] and (especially) following ultrasonication.

III. DATA PROCESSING AND MODELING

A. Data processing

In order to assist the study of aggregation, data from two automated event identification methods were reconciled. The *qNano* instrument control software registered events by identifying pulses exceeding a threshold (50 pA) from the baseline current, which was averaged over a time window (100 ms) adjacent to each event. The 50 pA threshold was of similar magnitude to the peak-to-peak electronic noise, whereas RMS noise did not usually exceed 15 pA. Event magnitude distributions and medians ($\sim$200 pA or greater, see Sec. IV) comfortably exceeded the threshold, indicating a good separation of event signals from the electronic noise. The second method used AXON CLAMPFIT software (v.10.1) to identify current pulses exceeding a user-defined threshold (independent of the baseline current) with event identification confirmed by visual inspection. Both methods efficiently identify resistive pulses for dispersed beads ($\Delta t \ll T$). For clustered events ($\Delta t \approx T$), the baseline current at the commencement of successive events is poorly defined, so discrimination between events using thresholding is impossible,

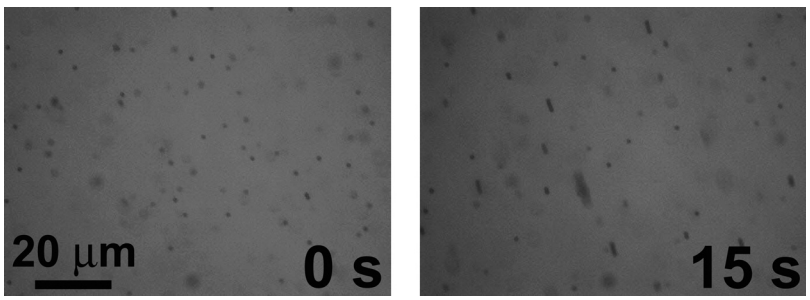

FIG. 2. Images of columnar SPS formation. Taken using an Axioskop 2 FS plus microscope with a non-immersion Zeiss LD Plan-Neofluar objective at 63 × magnification, numerical aperture 0.75. The bead-containing solution and placement of the bar magnet are consistent with the configuration in resistive pulse experiments.

although the second automated method allows identification of multiple or convoluted events during visual inspection. Automated data for clustered particles give a lower bound on the total number of particles passing through the pore.

B. Model

Resistive pulse simulations were carried out using a semi-analytic model.[34,35] Briefly, pore resistance is calculated by integrating the unobstructed pore area along the z-axis (Fig. 1(c)), assuming that the electrolyte resistivity is homogeneous and including the appropriate correction factor for a particle which is small in comparison with the pore size.[3,34,67] The simulations account for end effects and can calculate resistance when the particle is anywhere on the z-axis of any azimuthally symmetric pore. Particle transport is dominated by pressure-driven flow, where the volumetric flow rate Q is calculated using the approach of Dagan *et al.*[68] for a cylindrical channel of finite length. The pressure drop in a half-space beyond a pore opening of radius ω is given by Sampson flow,[69]

$$P_{out} = \frac{3\eta Q}{2\omega^3}. \tag{2}$$

Flow within the pore is approximately parabolic (Poiseuille), because the pore radius $R_P(z)$ varies slowly along the pore length, so

$$P_{in} = \int_0^d \frac{8\eta Q}{\pi R_P(z)^4} dz. \tag{3}$$

Beyond the membrane, on-axis transport is estimated by calculating the flow within an artificial cone, constructed to match the half-space pressure drop (Eq. (2)). This type of model has previously proved useful for exploring pulse magnitude and shape variations as a function of pore and particle geometry.[3,34,35] Similar approaches have been extensively applied in other resistive pulse studies.[15–17,23–25,28,70–72] For investigation of particle clusters, we extend the model to accommodate multiple on-axis particles, thereby improving on the established approach for sizing spheres using the proportionality of pulse magnitude and particle volume.[3,34]

The pore geometry used was a truncated cone of larger opening radius b, with a symmetric constriction of radius a located a distance c from the trans-membrane surface (Fig. 1(c)). This geometry can reproduce the asymmetry of experimental resistive pulses.[35] The pressure difference across the membrane was treated as an unknown in the model, along with a, b, and c. For a particular experiment, the data used to find these parameters were (1) the baseline resistance R_0, averaged across all recorded events, (2) the average pulse magnitude of 25 near-median events, (3) the full width quarter maximum (FWQM) event duration, and (4) fractional pulse asymmetry[35] at the FWQM, both averaged across 10 near-median events. Near-median events were used for calibration to ensure that data were representative of typical, individual pulses, and agreement with all four fitted parameters was obtained to better than 1%. During calibration, FWQM data were used in preference to full-width half maximum (FWHM) data (as used elsewhere) for increased precision.

IV. RESULTS

Table I summarizes the experiments, which were classified as reverse ("R") when $P_2 > P_1$, so that particles moved downwards through the pore; otherwise they were normal ("N"). In a typical experiment (Fig. 3(a)), the ionic current record commenced once steady events were observed with no magnetic field. A negative potential V_0 was applied, so the current is negative and pulses point in the positive direction. The initial stages of the current record act as the control mode ("C"), with the magnetic field applied later ("MP") and subsequently removed ("MR"). Data collected for each mode include at least 100 events in each normal experiment,

TABLE I. Summary of experimental data collected in three modes: prior to application of a magnetic field (control, "C"), with the magnet present ("MP") and with the magnet subsequently removed ("MR"). Blockages preclude comparison of all three regimes in most cases. Pressures include the contribution of the gravitational head. Event magnitude and FWHM duration are mean values for all identified events.

Experiment	$P_2 - P_1$ Pa ±20	Resistance MΩ ±0.02	Mode	Event rate s^{-1}	Magnitude nA	FWHM ms
N1	−569	1.19	C	10.8	0.47 ± 0.01	0.10 ± 0.01
			MR	37.9	0.71 ± 0.01	n/a[a]
N2	−569	0.74	C	11.6	0.33 ± 0.01	0.12 ± 0.01
			MP	15.6	0.39 ± 0.01	0.14 ± 0.01
			MR	14.9	0.41 ± 0.01	0.13 ± 0.01
N3	−372	0.74	C	5.2	0.27 ± 0.01	0.13 ± 0.01
			MR	23.7	0.24 ± 0.01	0.13 ± 0.01
N4	−372	0.72	C	10.7	0.40 ± 0.01	0.13 ± 0.01
			MP	17.3	0.57 ± 0.01	n/a[a]
			MR	156.6	0.45 ± 0.01	n/a[a]
N5	−274	0.62	C	16.1	0.20 ± 0.01	0.13 ± 0.01
			MP	16.3	0.26 ± 0.01	0.15 ± 0.01
N6	−372	0.51	C	19.3	0.17 ± 0.01	0.12 ± 0.01
			MP	31.6	0.20 ± 0.01	0.12 ± 0.01
R1	20	0.90	C	8.8	0.45 ± 0.01	0.60 ± 0.01
			MP	1.0	0.38 ± 0.02	0.49 ± 0.01
			MR	0.1	0.41 ± 0.01	0.54 ± 0.03
R2	20	0.88	C	0.5	0.30 ± 0.01	0.82 ± 0.03
			MP	0.0	0.26 ± 0.01	0.98 ± 0.05
R3	20	0.78	C	2.2	0.25 ± 0.01	1.16 ± 0.03
			MP	0.1	0.19 ± 0.01	0.90 ± 0.06
			MR	4.3	0.26 ± 0.01	1.17 ± 0.03
			MP	0.4	0.19 ± 0.02	1.23 ± 0.16

[a]Clustering prevents a meaningful average.

and a current record of at least 20 s in each reverse experiment. Data from transition periods were not analyzed due to mechanical transients caused by shifting the bar magnet. Pore blockages were clearly identifiable as discontinuous jumps in the baseline current, and/or cessation of recorded events. Such data were not analyzed, and blockages were removed between experiments by stretching the pore or by mechanically agitating the system. The degree of stretch applied to the pore is indicated by the pore baseline resistance. Current baseline drift did not typically exceed 0.015 nA s^{-1} and did not exceed 0.05 nA s^{-1} over any mode for any experiment. Drift is caused by viscoelastic mechanical creep of the pore shape[30] and transient capacitance following switching of the applied potential.

A. Upwards ("normal") transport

Experiment N4 (Fig. 3) demonstrates results which typify the trends observed in experiments N1-N6. In the control mode, dispersed particles passed freely through the pore. These events have consistent size and shape, rising more sharply than they fall (Fig. 3(b)), and they are widely distributed relative to the event width (Fig. 3(c)). The event rate increases following application of the magnetic field, and after 20 s events become densely packed, with increased magnitude. Close inspection of this region (Figs. 3(d) and 3(f)) reveals frequent resistive pulses with complicated, multi-peak structures, consistent with magnetic SPSs. Figure 3(e) shows typical events after the permanent magnet was removed—very frequent, and mostly dispersed into

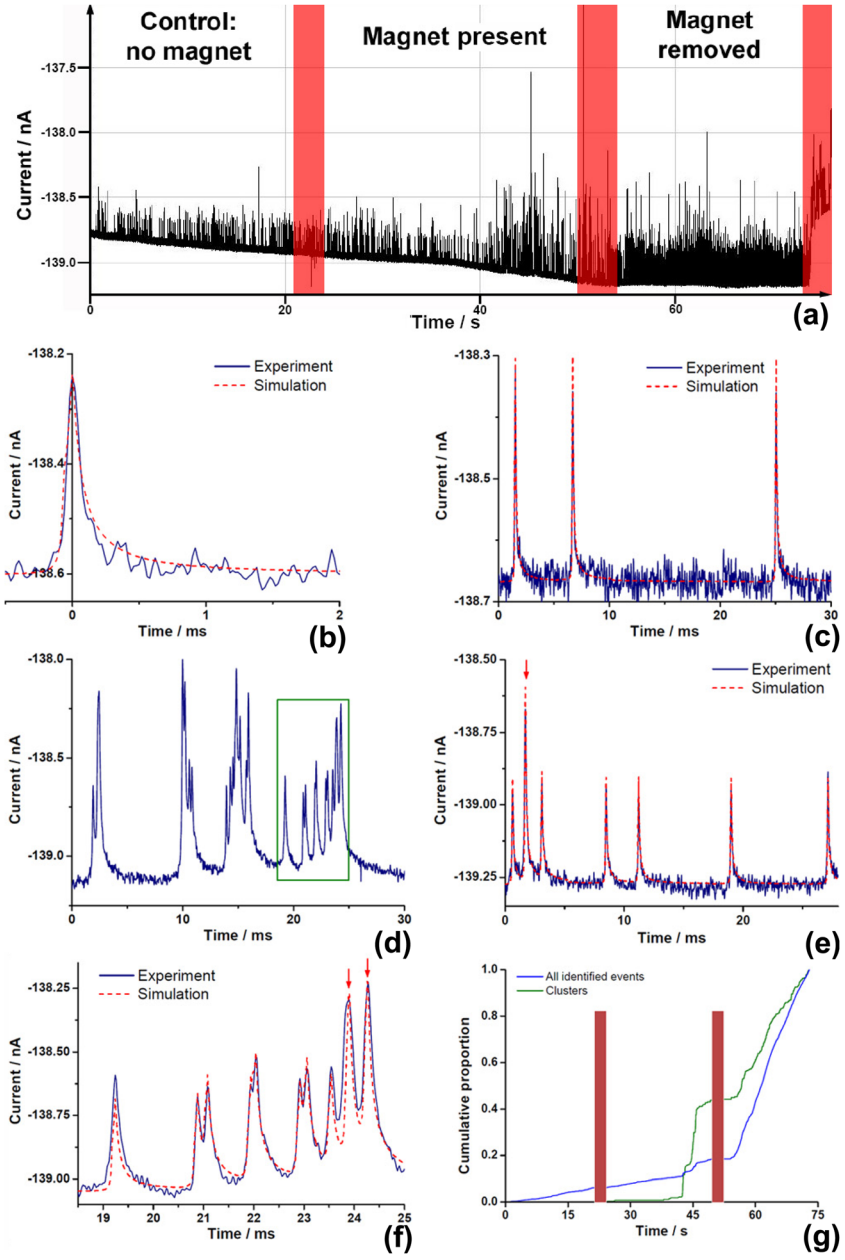

FIG. 3. Data for experiment N4: (a) The entire current record, with the magnetic field applied following the first highlighted in red region, and removed after the second such region. (b) The median magnitude event from the control region, and the simulated trace for control mode events. (c)–(e) Indicative resistive pulse patterns from "control," "magnet present," and "magnet removed" modes, respectively, while (f) is an expansion of the data within the green box in (d). Where simulations are plotted, red arrows indicate individual events identified as dimers. (g) The cumulative event count. As in (a), red bands indicate the changeover regions from where data were not collected. The total number of events was 3649, with 267 clusters identified using the automated method with visual inspection.

single peaks of consistent size and shape, but with some overlap into large or multi-peak events.

The cumulative event plot (Fig. 3(g)) is linear prior to application of the field ($R^2 = 0.999$), indicating a steady event rate. The rate increased discontinuously ~20 s after the magnet was applied. With the field removed, the rate was again linear ($R^2 = 0.995$), but much increased. "Cluster" events, identified while visually inspecting the peaks, have large and/or multi-peak structures not recognized by automated event identification methods. Figure 3(g) shows that

very few clusters occur when no magnetic field is applied, as expected for conventional resistive pulse experiments. After around 42 s, many clusters are observed, with rate irregularities corresponding to those in the overall rate. With the magnet removed, clusters are identified at a relatively steady rate, representing a lower proportion of the overall event rate than when the magnet was present. Clusters identified following removal of the field had relatively simple structures compared to those with the field applied (cf. Figs. 3(d)–3(f)).

Similar trends were observed in the other normal experiments (Table I). In each case, the event rate was greater than the control rate both with the field applied and after it was removed—albeit only marginally in experiment N5. With a magnetic field in place, either clustering or a pore blockage (or both) occurred, often following a delay. Blockages preclude clear comparison of all three regimes (as was possible for experiment N4) in most cases.

Interpretation of these trends is shown schematically in Fig. 4. Transport in the normal control case is dominated by pressure-driven flow, focused at the pore and acting upon an even distribution of beads. Following application of the magnetic field, particles begin to form SPSs and become more concentrated along the lower membrane surface, including near the pore entrance. There is a delay of ~20 s while this happens (Figs. 2 and 3(a)). With the field in place, clusters are detected as large, complicated, overlapping resistive pulses, occurring at an irregular rate due to steric interactions with each other and with the pore entrance. When the field is removed, events resume at a steady rate because the particles are mostly redispersed. However, the rate is higher than the control rate because of the raised concentration of particles near the pore entrance, where pressure-driven flow is focused. Some clustering is observed, either caused by remnant (hysteretic) magnetism in the particles[40] or stochastically, because the average duration of a single event is a reasonable fraction of the average time between events. In experiment N4, $\Delta t = 0.13$ ms (FWHM) and $T = 6.4$ ms following removal of the magnet.

1. Simulations

Simulated resistive pulses used in Fig. 3 were calibrated using typical events from the control region of experiment N4. Simulated pulses effectively reproduce the median pulse (Fig. 3(b)) when the baseline is shifted to match the event-specific baseline. The target baseline current, magnitude, FWQM width, and asymmetry were, respectively, 138.7 nA, 0.365 nA, 0.26 ms, and maximum current at 0.31 of the FWQM. The fitted values of a, b, and c were 2.4, 28.8, and 2.7 μm, respectively, with $P_2 - P_1 = -353$ Pa. These parameters are consistent with experimental values. Applied pressure was -372 ± 20 Pa, and pore openings can be imaged using scanning electron microscopy (SEM),[30,32–35] with specimens similar to the type used

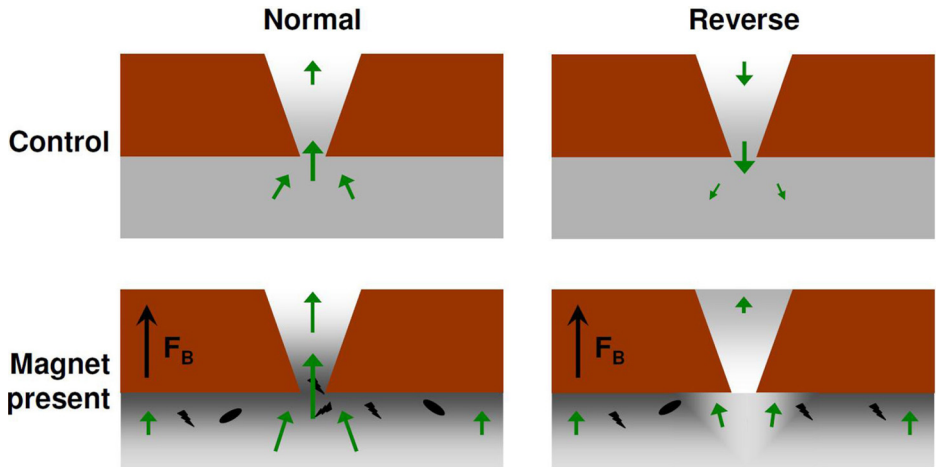

FIG. 4. Schematic diagrams (not to scale) indicating transport trends observed in experiments. Green arrows represent average velocity vectors of magnetic beads, bead concentration is indicated by grey shading, and small black objects represent formation of SPSs.

(classified NP1000 by Izon Science) having typical opening radii of 2.6 and 19.7 μm when the specimen arm length is extended to 45 mm.[73] A constriction below the pore surface is suggested by the membrane topography imaged by atomic force microscopy,[32] and this is not inconsistent with confocal microscopy[33] and SEM.[35] Closer comparison of fitted and experimental parameters would need to incorporate uncertainty in two further values, the electrolyte resistivity ($\rho = 0.75\ \Omega$ m) which is assumed homogeneous, and the membrane thickness (d = 159 μm), which is obtained using a hyperelastic material model of pore actuation.[31]

Fits to multiple peaks were generated by aligning simulated events with each experimental peak, and matching the baseline current with the local experimental background. There is a good agreement with experimental data in Fig. 3, and the simulations discriminate between events caused by dimers, as opposed to individual particles passing through the pore in quick succession. In Fig. 3(f), the simulated baseline current is fixed by matching the position of the final dimer peak, equivalent to a vertical shift of 0.097 nA from the experimental baseline. For rapid cluster detection, baseline currents are mismatched because the automated measurement does not account for detection of many particles in quick succession.

Further simulations of various bead structures are compared in Fig. 5. For contacting dimers and chains (Fig. 5(a)), individual beads are not distinguishable within each simulated event, although pulse magnitude and duration increase with increasing chain length. Figure 5(a) also shows that a pulse is larger, but narrower, when a dimer is rotated by 90°. For a ten-sphere chain, the current maximum occurs when most (approximately six) of the spheres lie below the constriction, giving rise to a change in peak asymmetry.

Figure 5(b) simulates events for two particles that are not in contact. It is assumed that each sphere moves independently in the flow field, so that when beads are at "close" approach (i.e., nearly touching) nearer to the pore constriction, they will be more closely spaced as they pass through the pore. Pulses for closely spaced particles can appear as wider, smaller magnitude versions of a contacting dimer. Particles become clearly distinguishable as their separation at the pore constriction is increased. Beads will further interact through the flow field, their magnetic dipoles, and surface forces, not considered here.

Many clusters detected in experiments had close but distinct peaks (e.g., Fig. 3(d)). Comparison with the peak spacing implied by independent bead trajectories (Fig. 5(b)) suggests that these beads were not touching when they passed through the pore. In contrast, columnar SPSs (Fig. 2) are predominantly formed by multiple contacting beads. The results, therefore, indicate that the columnar SPSs lose contact and become slightly separated as they pass through the

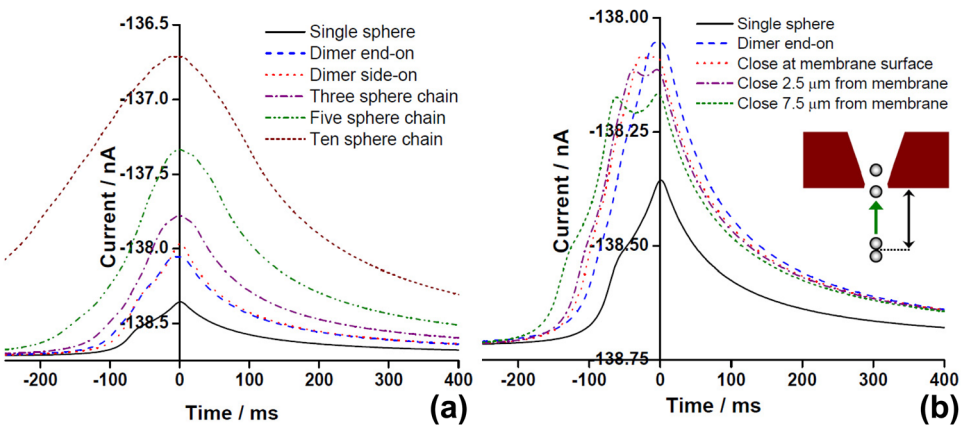

FIG. 5. Simulated resistive pulses, calibrated using parameters for the control mode in experiment N4. (a) Simulations of particle "chains" of various lengths translocating lengthwise, and for a dimer passing through the pore side-on. (b) Results for a single sphere and an end-on dimer with various cases in which two particles are transported independently of each other. Simulations are set up so that sphere surfaces are "close" (less than 50 nm apart) at some distance from the membrane surface. This distance is indicated by the black double arrow in the inset schematic section of the pore. Particles become more separated at the pore constriction, where the flow velocity gradient is maximized.

pore constriction. This observation is consistent with previous observations of chains breaking in shear flows,[56] and a similar scaling argument can be applied here, by considering the hydrodynamic (F_h) and magnetic (F_m) forces between the two spheres. F_h can be estimated using

$$F_h \sim 6\pi\eta a' \Delta v, \tag{4}$$

where a' is the particle radius and Δv is the difference in the flow velocity field at separations of 1 μm along the pore central axis—corresponding to the distance between adjacent bead centers. From the simulation with $P_2 - P_1 = -353$ Pa, the maximum value of Δv (at the pore constriction) is 13 mm s^{-1}. In the dipole approximation for the magnetic field,[74]

$$F_m = \frac{3\pi\mu_f a'^2 \beta^2 B^2}{2\mu_0 \mu_p^2}, \tag{5}$$

where B is the magnetic flux density, assumed parallel to the line joining the centers of the two spheres, and the force is attractive. μ_0 is the absolute permittivity of a vacuum, and μ_f and μ_p are the permeabilities of the fluid and the particle, respectively. The factor β is equal to $(\mu_p - \mu_f)/(\mu_p + 2\mu_f)$. For our experiments, the volume magnetic susceptibility of Dynabeads is $\sim$0.25 ($\mu_p \sim 1.25$),[75,76] μ_f is approximately 1 for water, and the magnetic flux density 15 mm from the polar face of the magnet used was 0.027 T, measured using a lakeshore 475 DSP Gaussmeter. Using these values, the ratio F_h/F_m (similar to the Mason number) was $\sim$50, consistent with the observed bead separation.

2. Methods for identifying aggregation

It is of interest to compare different methods for detection of particle clusters, or the onset of aggregation, during resistive pulse sensing. One such method involves monitoring the distribution of event magnitudes. In our normal experiments, the mean event size always increased when the magnet was present, by more than the standard error (Table I). Figure 6 compares event magnitude distributions for two experiments with apparently different aggregation characteristics. In experiment N4 (Fig. 6(a), similar to N1), aggregation was obvious: there is a marked difference in the distribution histogram, and 20%-30% of the events identified by the automated process were subsequently tagged as clusters during visual inspection. Clustered particles in contact (or near-contact) appeared as single or closely split peaks, with approximately double the magnitude of peaks for individual particles. Experiment N6 (Fig. 6(b), similar to N2) showed less clustering—only 1% or 2% of the events were clusters. Nevertheless, aggregation is apparent in the magnitude histogram. The modal peak has greater width with the field applied, and there is a clear increase in the proportion of "shoulder" events within the dashed green box. We can conclude that the event magnitude distribution has high sensitivity to

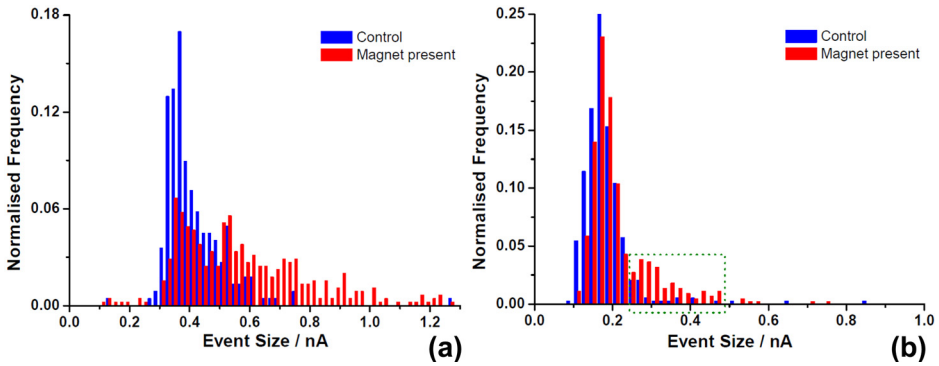

FIG. 6. Magnitude histograms for experiments N4 (a) and N6 (b) using data collected by the automated detection process. The dashed green box in (b) highlights a significant variation between the "control" and "magnet present" modes.

particle aggregation. This distribution can be compiled in real time using threshold-based automated detection, without detailed analysis of clustered events, and therefore provides a very efficient overall method for detecting aggregation.

There are other ways in which aggregation can be detected. The event rate can be monitored, and in our experiments the rate increases when the field is applied. However, this observation is particular to magnetic beads, whereas the magnitude distribution trend should generally apply to any aggregation process. Conversely, adhesion models for clustering[64] are not appropriate here due to magnetic interparticle interactions but could be useful in other aggregation studies using resistive pulse sensing. Another cluster analysis method compares the experimental distribution of times between successive events with the expected distribution for independent events. This stochastic distribution is monoexponential[77]

$$P_0(dt) = Ce^{-Rdt}, \tag{6}$$

where $P_0(dt)$ is the probability that following an event, zero events will occur in the time interval dt, C is a normalizing constant, and R is the average rate (number per second) at which events occur. According to Eq. (6), a log-linear plot of the normalized proportion of intervals between events as a function of dt should be linear, with a gradient of $-R$. In the plot for experiment N1 (Fig. 7(a)), in which extensive clustering occurred, the left-most data point deviates significantly from linear when the field is applied, indicating a large proportion of events that occur very close together in time. This is a signature for clustering, and clearly contrasts with the control data. For experiment N6, an increase in rate with the applied field is apparent, but there is no deviation from a linear trend. It is possible that a relatively high proportion of clusters passing through the pore in experiment N6 remain in contact, so that clustered beads are not recognized as being correlated. For aggregation investigations, this analysis of the time between events is less sensitive than observation of the magnitude distribution.

B. Top-to-bottom ("reverse") transport

In reverse experiments, transport was dominated by downwards flow from the gravitational head within the fluid cell—no pressure was applied to the system by the manometer. The direction in which a particle passes through the pore can be identified using the asymmetry of the resistive pulse (Ref. 35, Fig. 8). The majority of events occurred via top-to-bottom transport in reverse experiments, and observation of these events was serendipitous, because the hypothesis had been that only bottom-to-top transport would be observed, and only after the magnetic field was applied. Therefore, the solution introduced to the upper fluid cell did not contain SPMs, and few events (between 2 and 9 s^{-1}) were observed in the control mode. Beads that did pass through the pore were probably residual from earlier experiments, having persisted (perhaps within the cone of the pore itself) during rinsing and drying of the pore.

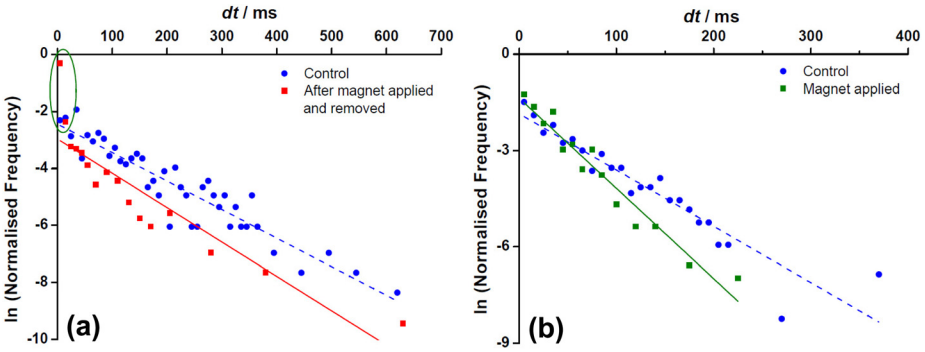

FIG. 7. The distribution of time between events for experiments N1 (a) and N6 (b), plotted against the natural log of normalized frequency. The straight lines are linear fits to the data, which were collected using the automated detection process. The green ring in (a) highlights data, which deviate significantly from the linear fit.

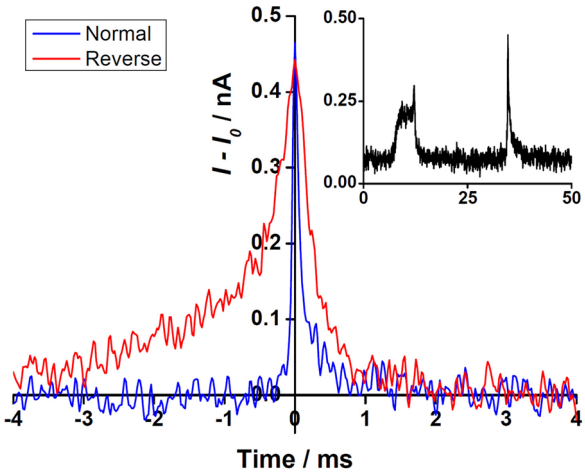

FIG. 8. Comparison of median events from control runs of experiments N1 and R1, which have respective peak heights of 0.46 and 0.44 nA, and FWHM widths of 0.12 and 0.58 ms. The measured current is plotted with the baseline current local to each event subtracted, and each peak has been shifted so that the maximum coincides with time = 0. Inset, normal and reverse events occur in quick succession with a magnetic field in place, indicating competing transport mechanisms.

Despite the relative paucity of data (Table I), reverse experiments provided some interesting observations. The mean FWHM duration was larger (Fig. 8) and more variable, ranging from 0.23 to 1.16 ms in control experiments, compared with a range of 0.10 to 0.13 ms for normal control experiments. Slow transport of particles through the pore is due to the pressure in the reverse configuration, which is a relatively small and opposes electrophoretic transport. There is a greater variation in the duration statistics because fractional uncertainty in the pressure is relatively large. Competition between transport mechanisms was also observed (Fig. 8), appearing comparable to variation of particle dynamics near the entrance to a ~150 nm diameter Si_3N_4 pore, recently observed using electrophoretically driven 85 nm silica spheres.[24]

In all reverse experiments, the event rate decreased with the magnet present, and experiment R3 suggests that the rate increases following removal of the field. Interpretation of the competing transport mechanisms is shown (alongside the normal case) in Fig. 4. In the reverse configuration, pressure-driven flow drives remnant particles downwards through the cone prior to application of the field. With the field applied, magnetophoresis opposes this pressure-driven flow, which is focused at the pore constriction. Transport of particles downwards from above the membrane and within the cone is slowed or reversed. Magnetic transport also dominates *below* the membrane, where there is a greater concentration of beads. However, magnetic transport is not focused at the constriction to the same extent as pressure-driven flow. For a homogeneous vertical magnetic field, the average downwards velocity of a bead is maximized at the constriction. The horizontal velocity below the membrane is directed away from the pore opening, so the bead concentration near this opening is depleted. Therefore, few (or no) bottom-to-top events are observed, despite dominance of upwards magnetophoretic transport over most of the system. No significant aggregation was observed in reverse experiments, because few events were observed at all with the magnet in place.

This interpretation is supported by an estimate of the relative contributions of the transport mechanisms. The magnetophoretic force on the bead is[40]

$$F_{mph} = \frac{V\chi}{\mu_0}(\mathbf{B}.\nabla)\mathbf{B}, \tag{7}$$

where χ is the volumetric magnetic susceptibility and V is the particle volume. In a dipole field, $\nabla\mathbf{B} \sim 3B/\alpha$, where α is the distance between the dipole and the particle, along the direction of the dipole. Equation (4) gives the hydrodynamic force, where the appropriate value for Δv here is the flow field velocity. Simulations indicate that the maximum velocity at the pore

constriction, which scales linearly with pressure, is around 50 mm s^{-1} when − 352 Pa is applied. The velocity in a half-space far from the constriction can be approximated by conserving the volume flow rate through a half-spherical surface. In the reverse configuration ($P_2 - P_1 = 20$ Pa), hydrodynamic and magnetophoretic forces are equal for beads approximately 80 μm from the pore constriction. When a bead is closer to the pore, focused pressure-driven flow is expected to dominate magnetophoresis.

Finally, we note secondary effects of electronic charge, not considered above. The DC dielectrophoretic force on a particle is[78]

$$F_{DEP} = 2\pi a'^3 \epsilon_m f_{CM} \left(\nabla E^2\right), \tag{8}$$

where ϵ_m is the electrolyte absolute permittivity and the magnitude of the electric field E can be calculated based on the modelled electric field.[34,35] Conservatively assuming highly conductive beads, so that the Claussius-Mossotti factor $f_{CM} \approx 1$, we estimate that F_{DEP} approaches 17% of the electrophoretic force at the pore constriction, where the electric field gradient is largest. F_{DEP} is directed towards the constriction, so pulse asymmetry could be slightly affected when pressure-driven flow is relatively small, as in "reverse" experiments.

The attractive force between induced dipoles on two separated spheres is[79]

$$F_{dipole} = 24\pi a'^6 \epsilon_m \left(\frac{D f_{CM} E}{D^3 - 2a'^3 f_{CM}}\right)^2, \tag{9}$$

where D is the distance between sphere centres. In a normal experiment, the force between particles in close proximity is greater than 20% of the estimated magnetic force (Eq. (5)) only when the particle moves to within ~1 μm of the constriction, where F_{dipole} is maximised. Away from the constriction, or when no magnetic field is applied, the experiments confirm that electric dipole attraction does not result in clustering comparable with magnetic SPS formation.

Streaming phenomena were not significant in this work. In a long cylinder with a thin double layer, the streaming current is approximately[80]

$$I_{stream} = \frac{\epsilon_m \zeta_{wall} A}{\eta} \frac{dP}{dz}, \tag{10}$$

where ζ_{wall} is the zeta potential at the cylinder wall and A is the sectional pore area. For our experiments, estimates of the corresponding streaming potential (conservatively using 20 μm pore radius, $\zeta_{wall} = 100$ mV, and the greatest applied pressure) give a value less than 0.1% of the applied potential.

V. CONCLUSIONS

Our experiments have demonstrated resistive pulse sensing of 1 μm magnetic beads using tunable pore technology. This appears to provide a very promising platform for detection of micro- and nanoparticle aggregation, particularly magnetic particle clustering in biosensing applications. Competition between transport mechanisms can explain comparative trends in the event rates when particles travel in both directions through the asymmetric pore, with and without a magnetic field applied. The field is near-uniform in comparison with pressure-driven flow, which is focused within and near the pore. Use of magnetophoresis as a switchable "body" force could provide a basis for controlling particle concentrations in resistive pulse sensing.

Particle dipole moments induced in the magnetic field also generate interparticle forces, and ultimately formation of SPSs. The onset of clustering was efficiently detected by monitoring the pulse magnitude distribution resulting from automated event identification. Data collected and analyzed in fewer than 5 min showed an increase in the mean pulse magnitude during clustering, raising the prospect of dynamic tracking of aggregation. Further information on clustering was drawn from the distribution of intervals between events, and comparison of

simulated events with the resistive pulse record. Simulations allow clusters of various sizes to be identified and distinguished from each other. Events caused by particles in contact with each other (or very close proximity) should appear as a single pulse, with a greater magnitude than the corresponding pulse for an individual particle. Numerous split peaks observed in the experimental record, therefore, suggest hydrodynamic separation of columnar magnetic SPSs as they moved through the pore, in agreement with scaling law calculations.

Future directions could include development of automated methods for identifying clusters within current histories, depending on the level of detail required for an application. Reconciliation of simulated and experimental baselines remains a difficulty, due to baseline drift and the cumulative effect of many events in a short space of time. Simulations could be expanded to account for interactions between beads, off-axis particles, and charge effects, which become important for smaller scale systems, or when the pressure difference across the sensing channel is small.

ACKNOWLEDGMENTS

This work was supported by The Royal Society of New Zealand's International Mobility Fund (Contract No. IMF10-B41). G.W. was supported by New Zealand's Ministry for Science and Innovation (NERF Contract No. C08X0806), and thanks staff at Izon Science and in Industrial Research Limited's Nano and Micro Fluidics team for assistance and useful discussions. M.P. was funded by an IEF Marie Curie fellowship Grant No. FP7-PEOPLE-2009-IEF (252935).

[1]W. H. Coulter, U.S. patent 2,656,508 (20 October 1953).
[2]R. W. DeBlois and R. K. A. Wesley, J. Virol. **23**, 227 (1977).
[3]R. W. DeBlois and C. P. Bean, Rev. Sci. Instrum. **41**, 909 (1970).
[4]J. J. Kasianowicz, E. Brandin, D. Branton, and D. W. Deamer, Proc. Natl. Acad. Sci. U.S.A. **93**, 13770 (1996).
[5]C. Dekker, Nat. Nanotechnol. **2**, 209 (2007).
[6]S. Benner, R. J. A. Chen, N. A. Wilson, R. Abu-Shumays, N. Hurt, K. R. Lieberman, D. W. Deamer, W. B. Dunbar, and M. Akeson, Nat. Nanotechnol. **2**, 718 (2007).
[7]J. Li, M. Gershow, D. Stein, E. Brandin, and J. A. Golovchenko, Nature Mater. **2**, 611 (2003).
[8]S. van Dorp, U. F. Keyser, N. H. Dekker, C. Dekker, and S. G. Lemay, Nat. Phys. **5**, 347 (2009).
[9]J. Mathe, H. Visram, V. Viasnoff, Y. Rabin, and A. Meller, Biophys. J. **87**, 3205 (2004).
[10]J. Clarke, H.-C. Wu, L. Jayasinghe, A. Patel, S. Reid, and H. Bayley, Nat. Nanotechnol. **4**, 265 (2009).
[11]D. W. Deamer and D. Branton, Acc. Chem. Res. **35**, 817 (2002).
[12]S. L. Cockroft, J. Chu, M. Amorin, and M. R. Ghadiri, J. Am. Chem. Soc. **130**, 818 (2008).
[13]E. H. Trepagnier, A. Radenovic, D. Sivak, P. Geissler, and J. Liphardt, Nano Lett. **7**, 2824 (2007).
[14]M. Firnkes, D. Pedone, J. Knezevic, M. Döblinger, and U. Rant, Nano Lett. **10**, 2162 (2010).
[15]S. W. Kowalczyk, A. Y. Grosberg, Y. Rabin, and C. Dekker, Nanotechnology **22**, 315101 (2011).
[16]D. Kozak, W. Anderson, R. Vogel, and M. Trau, Nano Today **6**, 531 (2011).
[17]T. Ito, L. Sun, and R. M. Crooks, Anal. Chem. **75**, 2399 (2003).
[18]T. Ito, L. Sun, M. A. Bevan, and R. M. Crooks, Langmuir **20**, 6940 (2004).
[19]G. Wang, B. Zhang, J. R. Wayment, J. M. Harris, and H. S. White, J. Am. Chem. Soc. **128**, 7679 (2006).
[20]R. An, J. D. Uram, E. C. Yusko, K. Ke, M. Mayer, and A. J. Hunt, Opt. Lett. **33**, 1153 (2008).
[21]G. Stober, L. J. Steinbock, and U. F. Keyser, J. Appl. Phys. **105**, 084702 (2009).
[22]L. J. Steinbock, G. Stober, and U. F. Keyser, Biosens. Bioelectron. **24**, 2423 (2009).
[23]W. J. Lan, D. A. Holden, J. Liu, and H. S. White, J. Phys. Chem. C **115**, 18445 (2011).
[24]L. Bacri, A. G. Oukhaled, B. Schiedt, G. Patriarche, E. Bourhis, J. Gierak, J. Pelta, and L. Auvray, J. Phys. Chem. B **115**, 2890 (2011).
[25]L. T. Sexton, L. P. Horne, and C. R. Martin, Mol. BioSyst. **3**, 667 (2007).
[26]J. E. Wharton, P. Jin, L. T. Sexton, L. P. Horne, S. A. Sherrill, W. K. Mino, and C. R. Martin, Small **3**, 1424 (2007).
[27]O. A. Saleh and L. L. Sohn, Nano Lett. **3**, 37 (2003).
[28]E. A. Heins, Z. S. Siwy, L. A. Baker, and C. R. Martin, Nano Lett. **5**, 1824 (2005).
[29]S. J. Sowerby, M. F. Broom, and G. B. Petersen, Sens. Actuators B **123**, 325 (2007).
[30]G. R. Willmott, M. F. Broom, M. L. Jansen, R. M. Young, and W. M. Arnold, in *Molecular- and Nano-Tubes*, edited by O. Hayden and K. Nielsch (Springer, Berlin, 2011), pp. 209–262.
[31]G. R. Willmott, R. Chaturvedi, S. J. W. Cummins, and L. G. Chaturvedi, "Actuation of tunable elastomeric pores: Resistance measurements and finite element modelling" (unpublished).
[32]G. R. Willmott and P. W. Moore, Nanotechnology **19**, 475504 (2008).
[33]G. R. Willmott, R. Vogel, S. S. C. Yu, L. G. Groenewegen, G. S. Roberts, D. Kozak, W. Anderson, and M. Trau, J. Phys.: Condens. Matter. **22**, 454116 (2010).
[34]R. Vogel, G. R. Willmott, D. Kozak, G. S. Roberts, W. Anderson, L. Groenewegen, B. Glossop, A. Barnett, A. Turner, and M. Trau, Anal. Chem. **83**, 3499 (2011).
[35]G. R. Willmott and B. E. T. Parry, J. Appl. Phys. **109**, 094307 (2011).
[36]G. S. Roberts, D. Kozak, W. Anderson, M. F. Broom, R. Vogel, and M. Trau, Small **6**, 2653 (2010).
[37]M. Low, S. Yu, M. Y. Han, and X. Su, Aust. J. Chem. **64**, 1229 (2011).

[38]R. Vogel, W. Anderson, J. Eldridge, B. Glossop, and G. R. Willmott, "A variable pressure method for characterising nanoparticle surface charge using pore sensors" (unpublished).
[39]Q. A. Pankhurst, J. Connolly, S. K. Jones, and J. Dobson, J. Phys. D: Appl. Phys. **36**, R167 (2003).
[40]M. A. M. Gijs, Microfluid. Nanofluid. **1**, 22 (2004).
[41]J. H. Chang, H. Shang, R. M. Perera, S.-M. Lok, D. Sedlak, R. J. Kuhn, and G. U. Lee, Analyst **133**, 233 (2008).
[42]B. B. Yellen, R. Erb, M. H. Son, S. R. Hewlin, H. Shang, and G. U. Lee, Lab Chip **7**, 1681 (2007).
[43]J. Prodelalová, B. Rittich, A. Spanová, K. Petrová, and M. J. Benes, J. Chromatogr. A **1056**, 43 (2004).
[44]K. Kang, J. Choi, J. H. Nam, S. C. Lee, K. J. Kim, S. W. Lee, and J. H. Chang, J. Phys. Chem. B **113**, 536 (2008).
[45]T. Kojima, Y. Takei, M. Ohtsuka, Y. Kawarasaki, T. Yamane, and H. Nakano, Nucleic Acids Res. **33**, e150 (2005).
[46]J. R. Whitaker, L. Zhao, H. Y. Zhang, L. Feng, D. Piening, L. Anderson, and A. Paulovich, Anal. Biochem. **1**, 44 (2007).
[47]J. S. Beveridge, J. R. Stephens, A. H. Latham, and M. E. Williams, Anal. Chem. **81**, 9618 (2009).
[48]N. Pamme, Lab Chip **7**, 1644 (2007).
[49]N. Pamme and C. Wilhelm, Lab Chip **6**, 974 (2006).
[50]R. Afshar, Y. Moser, T. Lehnert, and M. A. M. Gijs, Anal. Chem. **83**, 1022 (2011).
[51]M. Hoyos, L. Moore, P. S. Williams, and M. Zborowski, J. Magn. Magn. Mater. **323**, 1384 (2011).
[52]M. Hoyos, L. R. Moore, K. E. McCloskey, S. Margel, M. Zuberi, J. J. Chalmers, and M. Zborowski, J. Chromatogr. A **903**, 99 (2000).
[53]L. R. Moore, A. R. Rodriguez, P. S. Williams, K. E. McCloskey, B. J. Bolwell, M. Nakamura, J. J. Chalmers, and M. Zborowski, J. Magn. Magn. Mater. **225**, 277 (2001).
[54]K. H. Han and A. B. Frazier, J. Appl. Phys. **96**, 5797 (2004).
[55]S. Anandakumar, V. S. Rani, J. R. Jeong, C. Kim, K. W. Kim, and B. P. Rao, J. Appl. Phys. **105**, 07B312 (2009).
[56]I. Petousis, E. Homburg, R. Derks, and A. Dietzel, Lab Chip **7**, 1746 (2007).
[57]J. Baudry, C. Rouzeau, C. Goubault, C. Robic, L. Cohen-Tannoudji, A. Koenig, E. Bertrand, and J. Bibette, Proc. Natl. Acad. Sci. U.S.A. **103**, 16076 (2006).
[58]I. Koh, R. Hong, R. Weissleder, and L. Josephson, Anal. Chem. **81**, 3618 (2009).
[59]S. Y. Park, P. J. Ko, H. Handa, and A. Sandhu, J. Appl. Phys. **107**, 09B324 (2010).
[60]S. Y. Park, H. Handa, and A. Sandhu, Nano Lett. **10**, 446 (2009).
[61]J. Loureiro, R. Ferreira, S. Cardoso, P. P. Freitas, J. Germano, C. Fermon, G. Arrias, M. Pannetier-Lecoeur, F. Rivadulla, and J. Rivas, Appl. Phys. Lett. **95**, 034104 (2009).
[62]B. Zhang, M. Cho, J. B. Hughes, and J. H. Kim, Environ. Sci. Technol. **43**, 9124 (2009).
[63]W. G. Kreyling, M. Semmler-Behnke, J. Seitz, W. Scymczak, A. Wenk, P. Mayer, S. Takenaka, and G. Oberdörster, Inhalation Toxicol. **21**, 55 (2009).
[64]S. Trenor, K. Renshaw, M. Marek, K. E. Forsten, and B. Love, J. Adhes. Sci. Technol. **15**, 1189 (2001).
[65]R. L. Ryall, C. J. Bagley, and V. R. Marshall, Invest. Urol. **18**, 401 (1981).
[66]H. Y. Wang, Y. L. Ying, Y. Li, H. B. Kraatz, and Y. T. Long, Anal. Chem. **83**, 1746 (2011).
[67]E. C. Gregg and K. D. Steidley, Biophys. J. **5**, 393 (1965).
[68]Z. Dagan, S. Weinbaum, and R. Pfeffer, J. Fluid Mech. **115**, 505 (1982).
[69]R. A. Sampson, Philos. Trans. R. Soc. London **182**, 449 (1891).
[70]R. R. Henriquez, T. Ito, L. Sun, and R. M. Crooks, Analyst **129**, 478 (2004).
[71]R. Gasparac, D. T. Mitchell, and C. R. Martin, Electrochim. Acta **49**, 847 (2004).
[72]W. Sparreboom, A. van den Berg, and J. C. T. Eijkel, Nat. Nanotechnol. **4**, 713 (2009).
[73]L. Groenewegen, Izon Science, personal communication (2011).
[74]O. Volkova, S. Cutillas, and G. Bossis, Phys. Rev. Lett. **82**, 233 (1999).
[75]S. Reddy, L. R. Moore, L. Sun, M. Zborowski, and J. J. Chalmers, Chem. Eng. Sci. **51**, 947 (1996).
[76]C. B. Fuh, J. Z. Lai, and C. M. Chang, J. Chromatogr. A **923**, 263 (2001).
[77]A. Meller and D. Branton, Electrophoresis **23**, 2583 (2002).
[78]R. Pethig, Biomicrofluidics **4**, 022811 (2010).
[79]R. D. Stoy, J. Electrost. **33**, 385 (1994).
[80]B. J. Kirby and E. F. Hasselbrink, Jr., Electrophoresis **25**, 187 (2002).